Editors' Suggestion

Physical vapor deposition of Yb-doped $CsPbCl_3$ thin films for quantum cutting

Iver J. Cleveland, Minh N. Tran, Suryansh Kabra, Kajini Sandrakumar, Haripriya Kannan, Ayaskanta Sahu, and Eray S. Aydil*

Department of Chemical and Biomolecular Engineering, Tandon School of Engineering, New York University, Brooklyn, New York 11201, USA

(Received 17 February 2023; accepted 8 May 2023; published 7 June 2023)

Ytterbium-doped $CsPbCl_3$ is the leading candidate for a quantum-cutting coating on silicon solar cells to increase their efficiencies and durability by converting each incident ultraviolet and blue photon with energies >2.5 eV to two 1.25-eV near-infrared (NIR) photons. This approach can potentially increase silicon solar cell efficiencies above the Quessier limit. While photoluminescence quantum yields (PLQYs) approaching 200% have been demonstrated with thin films made using colloidal particle synthesis and nanocrystal dispersions, there is increased interest in physical vapor deposition as a large-area scalable method. We investigated the effect of Yb concentration and the annealing environment on the film structure, morphology, and optical properties, including the NIR PLQY. We found that subtle differences in the postdeposition annealing protocol significantly affect PLQY. Specifically, the highest PLQY (∼70%) is achieved by annealing the films in an N_2-filled glovebox first, followed by a second annealing step in air, both at 350 °C. X-ray photoelectron spectroscopy reveals that this approach anneals bulk defects, brings Yb to the surface, and forms a passivating oxide layer on the surface whose major component appears to be Yb_2O_3. Both surface oxidation and Yb segregation to the surface suppress grain growth during annealing. In addition, annealing only in air stops Yb segregation toward the surface. Annealing in N_2 brings Yb to the surface but does not form a robust oxide. In contrast, annealing in N_2, followed by annealing in air, brings Yb toward the surface and forms a passivating oxide, resulting in the highest PLQY.

DOI: 10.1103/PhysRevMaterials.7.065404

I. INTRODUCTION

All-inorganic metal halide perovskites have garnered significant attention as potential materials for solar cells, light-emitting diodes, photodetectors, and lasers because of their tunable band gaps [1,2], high absorption coefficients [3–6], and high photoluminescence (PL) quantum yields (PLQYs) [3,7–10]. Doping with intentionally added impurity atoms is a proven approach to modifying, improving, or imparting new functionality to these inorganic metal halide perovskites. For instance, rare-earth-doped inorganic halide perovskites are studied for optical downconversion, light emission, and quantum cutting [11–30]. In one of the most exciting applications for renewable energy generation, Yb-doped $CsPb(Cl_{1-x}Br_x)_3$ ($0 \leqslant x \leqslant 0.6$) is being pursued aggressively as a quantum-cutting coating on silicon solar cells to increase their operational lifetime and power conversion efficiencies [18,20]. Here, Yb-doped $CsPb(Cl_{1-x}Br_x)_3$ nanocrystal dispersions and films made from these nanocrystals have already exhibited quantum cutting with PLQYs exceeding 190% [14].

Quantum cutting is a form of *sensitized luminescence*, a phenomenon wherein an emitter, an impurity atom, is enabled to luminesce upon light absorption by the host (sensitizer) and subsequent transfer of all or some of the absorbed energy from the host to the emitter [31]. Specifically, quantum cutting refers to a phenomenon where the material absorbs a high-energy photon (E_{abs}) and then emits two low-energy photons (E_{emiss}) such that $2\,E_{emiss} \leqslant E_{abs}$. The energy transfer from the host to the emitter is possible if (i) the emission spectrum of the host overlaps the absorption spectrum of the sensitizer, (ii) there is an intermediate energy level, or (iii) the emission transition energy is half that of the sensitizer excitation transition [31–33]. For two photons to be generated, each by a different emitter, the emitters must be close, within ∼10−15 Å of the excited sensitizer, and have electronic transitions available with energies half that of the sensitizer [33]. The emitters act as traps for the exciton and, once excited, will either emit light or undergo a nonradiative transition [33]. Backtransfer of the energy from the emitter to the host lattice is unlikely because of relaxation effects [31].

Here, Yb^{3+} is an ideal luminophore for silicon photovoltaics because its $^2F_{5/2} \rightarrow {}^2F_{7/2}$ transition is 1.25 eV and is as good a match as one can have with the band gap of silicon [18,32]. A suitable Yb-doped host can be used as a quantum-cutting coating on silicon solar cells to increase their operational lifetime and power conversion efficiencies. This increase can be achieved by modifying the solar spectrum entering the solar cell by quantum-cutting high-energy blue and ultraviolet (UV) photons absorbed by the coating and generating two near-infrared (NIR) photons with lower energies close to the silicon band gap energy. Researchers have reported downconversion and quantum cutting with Yb codoped with another rare-earth element in various optically passive insulator hosts [34–36]. One of the issues with this codoping

*aydil@nyu.edu

method to achieve quantum cutting is that the absorption spectra of many of the frequently used sensitizing rare-earth elements are quite narrow and weak due to forbidden f-f transitions [36,37]. Relying on narrow bandwidth absorption of rare-earth codopants in insulating hosts severely limits the effectiveness of quantum-cutting and downconverting layers on solar cells [38]. For practical applications, broadband sensitization is desirable. Several semiconducting hosts with broadband interband absorption, including $CsPbX_3$ (X = Cl, Br), $NaInS_2$, and CdSe, have been studied for sensitizing Yb^{3+} [11,27,39]. Among these Yb-doped $CsPb(Cl_{1-x}Br_x)_3$ nanocrystals have been the most successful, showing PLQY approaching 200% [14].

A host material band gap of at least 2.5 eV is required to excite two Yb^{3+} ions to emit two 1.25 eV NIR photons with a single >2.5 eV photon absorption [13]. The $CsPb(Cl_{1-x}Br_x)_3$ band gap ranges from 2.25 eV ($x = 1$) to 3 eV ($x = 0$) depending on the halide composition (x), which can be easily varied during synthesis either by selecting the appropriate ratios of Cl^-- and Br^--containing precursors or via anion exchange. Here, $CsPb(Cl_{1-x}Br_x)_3$ is a suitable Yb^{3+} host when its band gap is wider than 2.5 eV which corresponds to Cl concentrations >35% Cl ($x \leqslant 0.65$). Most research on Yb-doped $CsPb(Cl_{1-x}Br_x)_3$ has been conducted on nanocrystals made using colloidal synthesis, which consistently yields high PLQYs approaching 200% [12,14–16,27,28,40–46]. The highest PLQYs have been achieved in nanocrystal dispersions or thin films with band gaps of ≈2.5 eV (≈35% Cl and 65% Br) [13,14,43]. Here, Yb-doped $CsPb(Cl_{1-x}Br_x)_3$ NIR PLQY remains constant for band gaps from ∼ 3 to 2.5 eV and then decreases precipitously once the band gap is lowered below the 2.5 eV threshold [13]. Most reports show that PLQY increases with Yb concentration in the ∼ 0−10% range reported in percent of the Pb lattice positions (i.e., $\%Yb[Yb]/([Yb]+[Pb]) \times 100\%$) [47]. In this paper, Yb concentrations are also reported in percent of Pb lattice positions.

There is evidence that, in moderate concentrations (e.g., <2.71%), Yb substitutes into Pb lattice positions (Yb_{Pb}) in the crystal structure [48]. Two Yb^{3+} ions must replace three Pb^{2+} ions to maintain charge neutrality, resulting in a Pb vacancy V_{Pb}. Figure 1 depicts a defect complex comprising two Yb_{Pb} and a V_{Pb} suspected of facilitating quantum cutting [12,49,50]. The thinking is that the exciton is trapped by this defect which conveniently has two Yb^{3+} ions for (each) receiving half the exciton energy. The formation energies of various Pb-vacancy-related defects were studied recently by Sommer *et al.* [22], who found that Yb_{Pb} is a shallow donor, but $(Yb_{Pb} + V_{Pb})^-$ and $(2Yb_{Pb} + V_{Pb})^\circ$ complexes are deep acceptor levels near the conduction band minimum with $(2Yb_{Pb} + V_{Pb})^\circ$ being more stable because it is charge neutral. The close spatial coupling between the two Yb_{Pb} and a V_{Pb} in a complex is consistent with Dexter's [31] estimate that the emitters must be close, within ∼12 Å of the excited sensitizer, in this case, the exciton trapped at the defect. Sommer *et al.* [22] also found that, at Yb-doping concentrations >1%, most Yb ions are within 12 Å of each other, the quantum-cutting sensitization distance cutoff predicted by Dexter [31], and long-range Coulomb interactions form $Yb_{Pb}-V_{Pb}$ complexes.

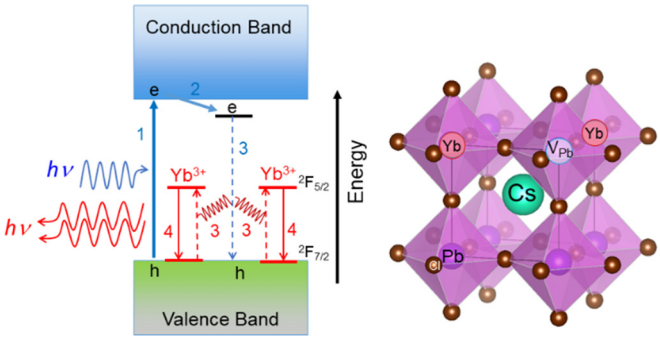

FIG. 1. The hypothesized mechanism of quantum cutting in $CsPbCl_3$ with the energy diagram on the left and a $Pm\bar{3}m$ $CsPbCl_3$ cubic unit cell (stable T>46 °C) with a defect complex comprising two Yb_{Pb} substitutional defects and a Pb vacancy V_{Pb} on the right. The defect is illustrated using the cubic structure for clarity. At room temperature, the stable $CsPbCl_3$ structure is orthorhombic (*Pnma*) in which the octahedra are tilted. On the right, (1) a blue photon is absorbed to create an exciton which is then (2) trapped in a defect. (3) The exciton transfers the energy to two nearby Yb^{3+} ions, exciting them from the $^2F_{7/2}$ ground state to the excited $^2F_{5/2}$ state. (4) The excited Yb^{3+} ion relaxes and emits two near-infrared (NIR) photons (∼1.25 eV). Yb^{3+} levels are placed superimposed on the band diagram for illustration purposes only [49,50].

The highest NIR PLQY values have been obtained from Yb-doped $CsPb(Cl_{1-x}Br_x)_3$ nanocrystal dispersions produced using colloidal synthesis approaches and from films formed by spin-coating and annealing solutions containing the precursors. However, these methods suffer from the problems associated with solution-based and colloidal halide perovskite synthesis, for instance, precursor solubility and scalability: CsX and PbX_2 have limited solubility in the same solvent and must be spun-cast in two steps. In addition, controlling Yb concentration and incorporating high Yb concentrations (e.g., >7%) into $CsPb(Cl_{1-x}Br_x)_3$ nanocrystals have been difficult in solution-based synthesis. Two approaches to avoid these problems have been two-step spin coating and single-source vapor deposition from Yb-doped $CsPb(Cl_{1-x}Br_x)_3$ powders [13,17,19,47,51]. Two-step spin coating and single-source vapor deposition have achieved PLQYs as high as 193 and 183%, respectively. In the two-step spin coating, a layer of PbX_2 is first deposited, followed by a layer of CsX and YbX_3 solution. The resulting two-layer coating is annealed to form the Yb-doped $CsPb(Cl_{1-x}Br_x)_3$ film. The film halide composition can be tuned by varying the ratios and concentrations of Cl- and Br-containing precursors in the deposition solutions. This is particularly useful because the perovskite band gap is easily tuned to the ideal band gap of ∼2.5 eV, and the Yb content is easily varied by changing the ratio of Cs:Yb with Yb doping as high as ∼54% being demonstrated by Ishii and Miyasaka [51], though it is not clear if all this Yb is substitutional or ends up in the grain boundaries. While solution-based techniques have achieved PLQYs approaching 200% in colloidal dispersions and films cast from them, difficulties in scalability, precursor solubility, and sub-band-gap absorption limit their commercialization.

Physical vapor deposition (PVD) by evaporation is an alternative to solution-based methods for synthesizing halide

perovskite thin films. While PVD has been used widely for depositing various halide perovskites, to date, only single-source vapor deposition of Yb-doped $CsPbCl_3$ has been demonstrated [17,19]. Single-source deposition requires forming the perovskite via another method and evaporating it onto the substrate. PVD of Yb-doped $CsPbCl_3$ from a single source is difficult because it is unclear if $CsPbCl_3$ can be evaporated congruently at slow and controllable rates (∼1 Å/s) that lead to reproducibly high-quality films. Previous work used flash evaporation (∼1000 Å/s deposition rate) to achieve the same film composition as the source material, but flash evaporation is difficult to control to achieve high-PLQY reproducibly [17]. Multisource evaporation is an alternative approach that affords more flexibility in tuning the film stoichiometry. Precursor salts (e.g., CsCl, $PbCl_2$, and $YbCl_3$) are evaporated simultaneously (coevaporation) or sequentially using multiple sources. These precursors react on the substrate either during deposition (depending on the substrate temperature) or during a postdeposition annealing step.

Herein, we report on the effects of coevaporation parameters on the PLQY of Yb-doped $CsPbCl_3$ thin films. Specifically, we investigated the effects of film stoichiometry, Yb concentration, substrate temperature during deposition, and postdeposition annealing conditions such as annealing duration, temperature, and environment. All Yb-doped films showed emission from the Yb $^2F_{5/2} \rightarrow {}^2F_{7/2}$ transition centered at 985 nm. We demonstrate Yb-doping as high as 10% and NIR PLQY as high as 70%. Visible PL and UV-vis absorption onset show that the films have a band gap of ∼2.95 eV. X-ray diffraction (XRD) spectra show that the films are phase-pure $CsPbCl_3$ with no noticeable shift in peak positions with increasing Yb concentration. Scanning electron microscope (SEM) images show the incorporation of Yb severely limits grain growth. Annealing $CsPbCl_3$ thin films in the air with or without Yb also limits grain growth in the films. X-ray photoelectron spectroscopy (XPS) measurements provide insight into the effects of the annealing environment on the location of Yb ions and the importance of their position within the film, with Yb being present on the surface of films annealed in air-free environments but being absent from the surface of films annealed solely in air.

II. EXPERIMENTAL

Here, Yb-doped $CsPbCl_3$ thin films were deposited in a gloveboxed (GB) PVD system (Angstrom Engineering) with six evaporation sources and equipped with a masking shutter (Fig. 2). The shutter comprises two knife edges whose positions can be translated close to the substrate to expose regions with predetermined widths (typically 25 mm in this paper). The rotatable substrate stage can accommodate nine 25 × 25 mm substrates, as shown in Fig. 2. The substrate holder is heated with circulating fluid, and its temperature is controlled between 25 and 200 °C with a closed feedback loop comprising a thermocouple and a controller. The substrate temperature has been calibrated with respect to the circulating fluid temperature, and the temperatures reported herein are the substrate temperatures. In typical experiments discussed herein, nine 25 × 25 mm glass substrates were loaded onto the substrate holder, and triplicates of 25 × 25 mm samples

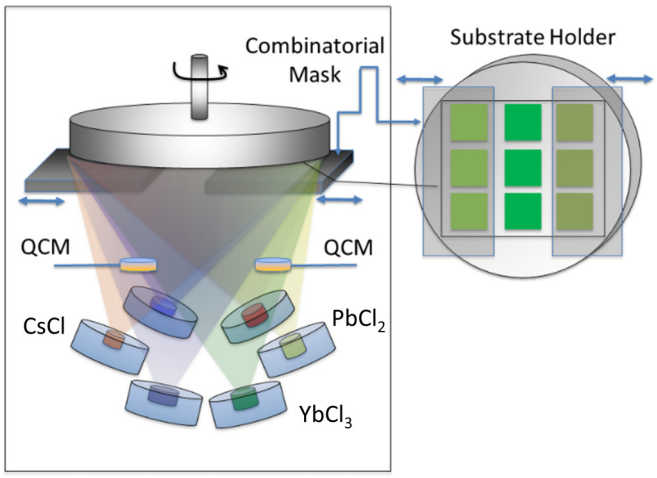

FIG. 2. Schematic illustration of the physical vapor deposition (PVD) system and the masking shutter. QCM: quartz crystal microbalance.

were deposited by positioning the shutter over a 25-mm-wide column. This way, a deposition parameter, such as the ratio of precursor fluxes, could be changed, and three different values could be explored at the same deposition temperature in a single deposition experiment.

In typical experiments, the powders of the three precursors, CsCl (99.9% Alfa Aesar), $PbCl_2$ (99.999 Sigma Aldrich), and $YbCl_3$ (99.9% Alfa Aesar), were packed into separate alumina crucibles and loaded into three of the six RADAK evaporation sources. The glass substrates (25 × 25 mm) were cleaned by sonicating for 10 min in a 1:1 (by volume) solution of acetone and isopropanol and dried in an oven before loading into an ozone plasma cleaner. The substrates were exposed to ozone plasma for 20 min before loading into the substrate holder. The deposition rates for CsCl, $PbCl_2$, and $YbCl_3$ were measured by separate quartz crystal microbalances (QCMs) and, in most of the experiments reported here, maintained at 0.89, 1.0, and 0–0.16 Å/s unless noted otherwise. A closed-loop feedback controller maintained the deposition rates at the set point to within 2%. The tooling factors for CsCl, $PbCl_2$, and $YbCl_3$ (deposition rate/deposition rate at the QCM in %) were 39.7, 39.3, and 39.7, respectively (see below and the Supplemental Material [52] for details). These evaporation rates result in a molar flux ratio of 1:1 for CsCl and $PbCl_2$. Off-stoichiometric films were deposited by varying the evaporation rate of CsCl. Here, Pb-rich films were formed by decreasing the CsCl rate to 0.8 Å/s, and Cs-rich films by increasing the CsCl rate to 0.98 Å/s. The evaporation rate controller manipulates the source temperatures to maintain the deposition rate at the set point. Thus, the temperatures of the CsCl, $PbCl_2$, and $YbCl_3$ sources were manipulated to keep the deposition rate constant but were ∼600, 350, and 700 °C, respectively, except for small fluctuations, up or down, to maintain the deposition rates constant at their set points within 2%. The deposition time for the films was 2000 s. The deposition chamber base pressure is $\approx 10^{-8}$ Torr which typically rises to $\approx 10^{-6}$ Torr during the deposition. After the deposition, the films were annealed on a hotplate set to 250, 300, 350, or 400 °C either in an N_2-filled GB for 2 h

or in the air for 2 h. Films were also annealed first in the GB for 2 h and then in the air for 2 h for a total of 4 h. The hotplate was preheated before the films were placed on it and remained at that temperature for the annealing duration until after the films were removed and allowed to cool while off the hotplate. Films were kept in the GB before annealing. Annealing was typically started after 1 h of taking them out of the PVD chamber vacuum into a nitrogen-filled GB. The annealing protocols were kept consistent across all samples.

The thicknesses of the $CsPbCl_3$ and $PbCl_2$ films were determined from the thin-film interference fringes in the optical transmission data at energies below the band gap energy (e.g., $<$2.95 eV for $CsPbCl_3$). A model based on the Fresnel equations and valid for transparent thin films on a semi-infinite transparent substrate was used to fit the interference fringes appearing in the optical transmission data and using the published refractive indices for $CsPbBr_3$ [53] and $PbCl_2$ [54]. The model and fitting procedure are described in detail in the Supplemental Material with example fits (Figs. SI1 and SI2) [52]. The nominal targeted thickness was ~375 nm, and the range of all film thicknesses was 350–400 nm. Sources of error include scattering and absorption, which decrease the fit quality of the optical model. Optical models and thicknesses obtained from scanning electron micrographs produce the same thickness within experimental error.

All films were characterized under ambient conditions. XRD patterns were collected using a Bruker AXS D8 Discover GADDS microdiffractometer equipped with a Cu-Kα source. The XRD spot is elliptical with an approximate average size of 800 μm. The samples were oscillated in two orthogonal directions to average the data over a $2 \times 2\,\mathrm{mm}^2$ area. Optical absorption by the films was measured using an Agilent Cary 5000 UV-Vis-NIR spectrometer in the range of 300–2000 nm. PL was excited between 300 and 400 nm (5-nm bandwidth) using a 75 W Xe arc lamp filtered by a double monochromator and detected, after filtering with a single monochromator, using an infrared intensified R13456 photomultiplier tube (Hamamatsu) in a Horiba Quantamaster fluorometer. Films were examined using an Oxford Instruments Merlin field emission SEM (5 kV, 110 pA). Their average elemental composition, over ≈10 $\mu\mathrm{m}^2$, was determined using energy-dispersive x-ray spectroscopy (EDS) and vendor-provided sensitivity factors. Physical Electronics Versaprobe II XPS was used to identify the electronic valence state of the elements in Yb-doped $CsPbCl_3$ ($CsPbCl_3$:Yb). The Al-Kα source was operated at 50 W and 15 kV with an energy resolution of 0.25 eV/step and 200 μm spot size to probe the thin films. All high-resolution element-specific spectra were obtained with a pass energy of 29.35 eV, while survey scans were taken at 117.4 eV pass energy and 1 eV/step, with 100 ms time per step. Multiple scans were averaged to improve the signal-to-noise ratio: carbon (3 sweeps); Cs and Pb (5 sweeps); and Cl, Yb, and O (15 sweeps). Before acquiring XPS data, a $3 \times 3\,\mathrm{mm}^2$ area was sputtered for 15 s with 5 keV Ar^+ ions. Spectra were collected before and after sputtering, the major difference being the reduction in adventitious carbon in the spectra taken after sputtering. XPS peaks were fit by first subtracting either a Shirley, linear, or polynomial background from an appropriate spectrum region for each elemental peak. After the background subtraction, we fitted the spectra with one or more Gaussian functions by varying the peak area, peak center, and width. For peaks with spin-orbit splitting, the area ratios for the two components were fixed to appropriate values for the orbital.

III. RESULTS AND DISCUSSION

A. Effect of annealing environment on the PLQY

We investigated the effects of Yb concentration and the annealing environment on the film structure, morphology,

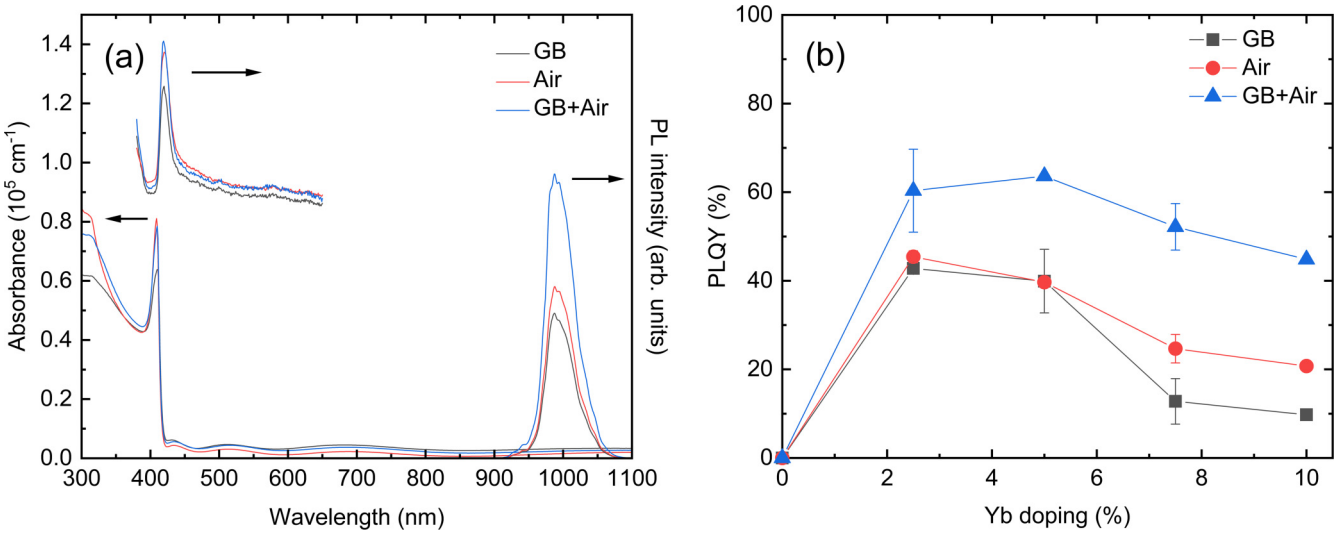

FIG. 3. (a) Optical absorption, visible, and near-infrared (NIR) photoluminescence (PL) from stoichiometric $CsPbCl_3$ films (Cs:Pb = 1) doped with 5% Yb and annealed in three different ways: (1) in a nitrogen-filled glovebox (labeled GB) for 2 h, (2) in the air for 2 h (labeled Air), and (3) in a nitrogen-filled GB for 2 h, followed by further annealing in the air for another 2 h (labeled GB+Air). The annealing temperature was 350 °C. The visible and NIR PL intensities in (a) are in arbitrary units (arb. units), but the NIR PL peak intensity is scaled with the PLQY value of the corresponding film. (b) Yb-concentration dependence of NIR PLQY for stoichiometric $CsPbCl_3$ films (Cs:Pb = 1) annealed in three different ways.

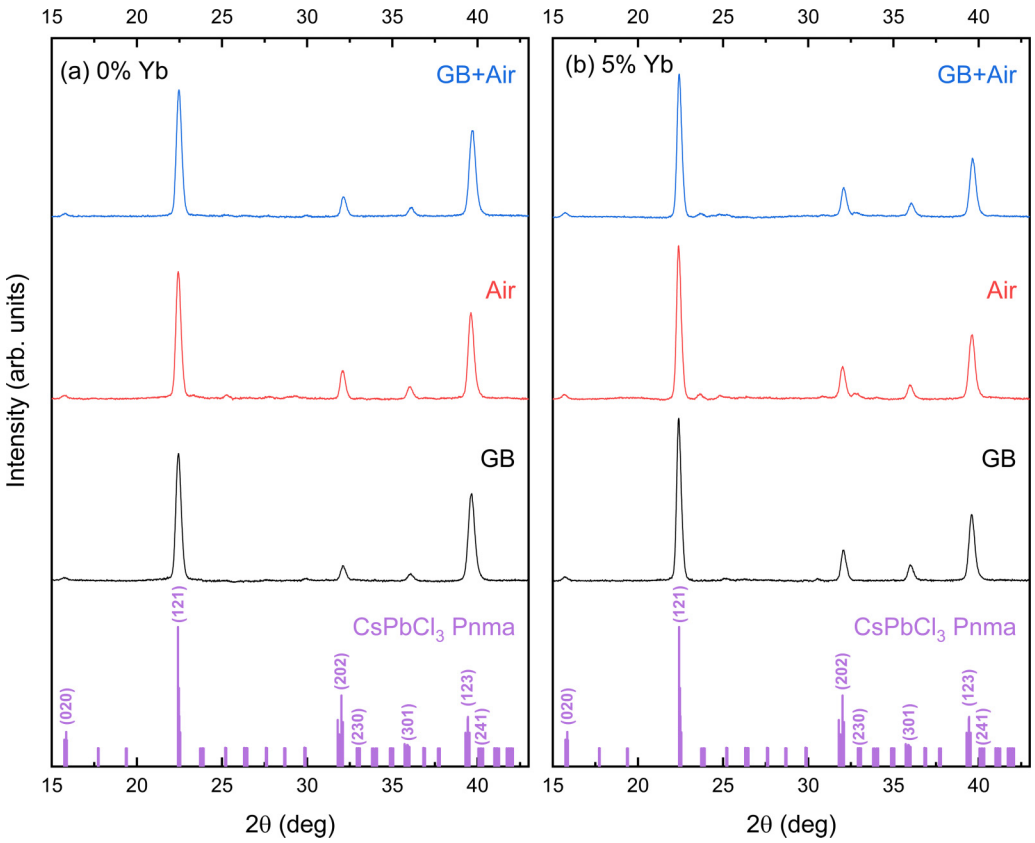

FIG. 4. X-ray diffraction (XRD) from (a) undoped and (b) 5% Yb-doped stoichiometric $CsPbCl_3$ films annealed in three ways as labeled in the Fig. 3 caption. The powder diffraction pattern, calculated using VESTA software and the crystallographic information file (CIF) from Ref. [50] for the orthorhombic *Pnma* $CsPbCl_3$ structure, is shown for comparison [49,50].

and optical properties, including the NIR PLQY. Figure 3(a) shows the optical absorption and PL spectra of the stoichiometric $CsPbCl_3$ film doped with 5% Yb. The PL was excited at 360 nm with 5-nm bandwidth. Optical absorption and PL for all other films deposited using slightly different Cs:Pb ratios (±10% deviations from stoichiometry) and Yb concentrations are in the Supplemental Material (Figs. SI3 and SI4) [52]. Data are shown for films annealed in three ways: (1) in a nitrogen-filled GB for 2 h (hereafter labeled GB), (2) in the air for 2 h (labeled as Air), and (3) in a nitrogen-filled GB for 2 h, followed by further annealing in the air for two more hours (labeled GB+Air). The absorption shows the expected and well-known exciton peak at ∼3 eV (410 nm) and does not change significantly with the annealing environment or Yb concentration. Here, Cs-rich films (Cs:Pb = 1.1) are slightly redshifted (5 nm) from the stoichiometric (Cs:Pb = 1) and Pb-rich (Cs:Pb = 0.9) films (Fig. SI3 in the Supplemental Material [52]). The exciton PL (420 nm) from Yb-doped films is weak, and PLQY is <1%, the detection limit in our integrating sphere, independent of how the films are annealed. However, the NIR PLQY from the $^2F_{5/2} \rightarrow {}^2F_{7/2}$ transition (985 nm) in Yb is high, 40% for the GB and air-annealed films and 64% for films first annealed in the GB and then in the air [Fig. 3(b)]. NIR PLQY was maximized with an annealing temperature of 350 °C for GB-annealed 5% Yb films (Fig. SI5 in the Supplemental Material [52]). Annealing films with 5% Yb for 2 or 4 h in a GB result in comparable NIR PLQY (Fig. SI6 in the Supplemental Material [52]). This is also an important control for distinguishing between the effect of annealing time and the annealing environment. Without this comparison, the differences in PLQY from films annealed in GB for 2 h and films annealed in GB for 2 h followed by 2 h in the air could be explained by the differences in annealing time. Figure 3(b) shows the PLQY as a function of Yb concentration for stoichiometric films (Cs:Pb = 1) annealed in three different ways. Similar plots for films deposited using slightly different Cs:Pb ratios (±10% deviations from stoichiometry) are shown in Fig. SI4 in the Supplemental Material [52]. For all Yb concentrations and small deviations of Cs:Pb ratios from stoichiometry, films annealed in N_2 followed by annealing in the air had higher PLQY than films annealed solely in the GB or the air. PLQY of films annealed only in N_2 increased 5–10% (absolute PLQY) after 3–5 days of air exposure, indicating that oxidation may passivate surface defects in the films. We surmise that annealing films in the air after annealing them in the GB makes this oxidation and surface-defect passivation more complete, controllable, and robust than aging the film in the air. The highest PLQY achieved was 69.7% in stoichiometric films (Cs:Pb = 1) doped with 2.5% Yb. Here, Pb-rich films (Cs:Pb = 0.9) showed a similar trend, with the highest PLQY of 63.2% coming from a film with 2.5% Yb doping (Fig. SI4(b) in the Supplemental Material [52]). PLQY decreased as Yb concentration increased >5%. This decrease could be due to concentration quenching.

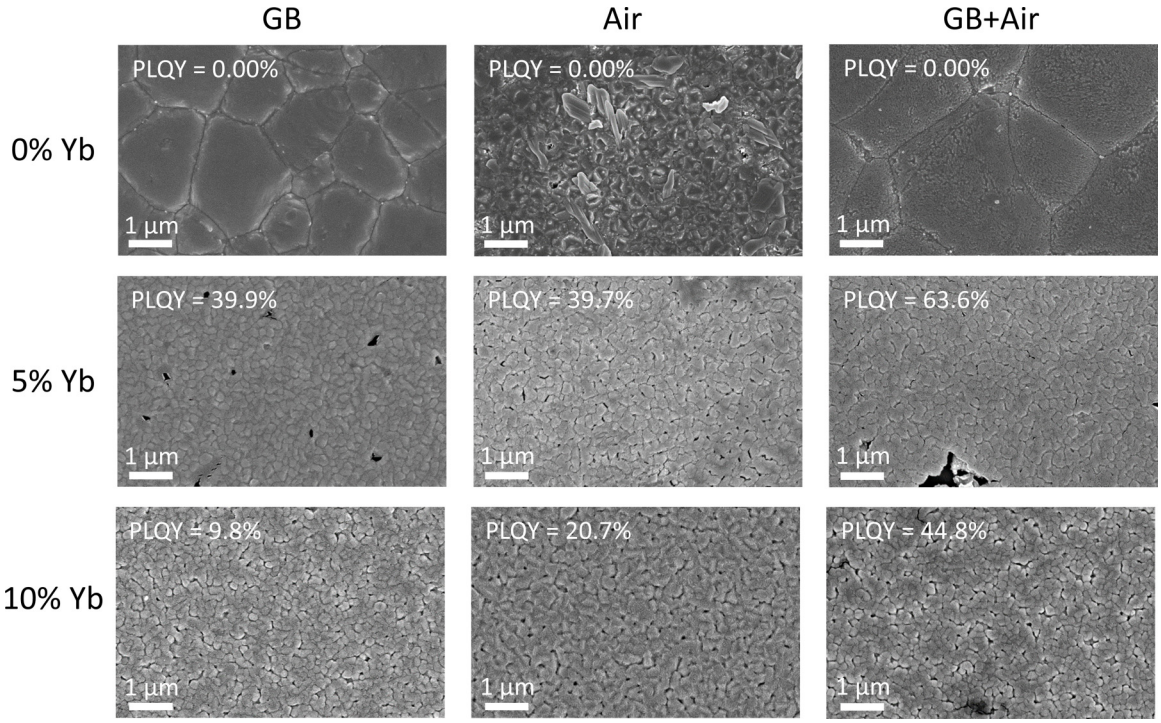

FIG. 5. Scanning electron microscope (SEM) images and average photoluminescence quantum yield (PLQY) of undoped and Yb-doped (5 and 10%) stoichiometric $CsPbCl_3$ films annealed in three ways as labeled in the Fig. 3 caption. See Fig. SI12 in the Supplemental Material [52] for stoichiometric films with 2.5 and 7.5% Yb concentrations and Figs. SI13 and SI14 in the Supplemental Material [52] for films deposited with Cs:Pb ratios 0.9 and 1.1, respectively.

B. Effect of annealing environment on film structure and morphology

Figure 4 shows the XRD patterns for stoichiometric $CsPbCl_3$ films with no Yb and 5% Yb doping. XRD patterns for other Yb concentrations and off-stoichiometric films are in Figs. SI7–SI11 in the Supplemental Material [52]. The XRD from the $CsPbCl_3$ films is consistent with the equilibrium orthorhombic (*Pnma*, #62, $a = 7.902$ Å, $b = 11.248$ Å, $c = 7.900$ Å) structure [50]. XRD peaks do not shift significantly when the films are doped with Yb. Comparison with the powder diffraction pattern shows that the films are textured. Moreover, XRD patterns of films with the same composition annealed in different environments have nearly identical patterns.

Figure 5 shows the SEMs of undoped $CsPbCl_3$ films and films doped with 5 and 10% Yb. Figure 5 also shows the effect of annealing these films in three ways (GB, Air, and Air+GB; SEMs of films at other Yb-doping levels and Cs:Pb ratios are shown in Figs. SI12–SI14 in the Supplemental Material [52]). The annealing environment and Yb doping strongly affect the microstructure of the film. SEM images of undoped $CsPbCl_3$ films annealed in the N_2-filled GB show easily distinguishable 1–2-µm-size grains, while the grains of undoped films annealed in the air are much smaller ($\sim 100 - 300$ nm) and less distinct. We attribute the smaller grain size in the air-annealed films to oxygen passivation of grain boundaries restricting grain growth. The films annealed in the GB followed by annealing in the air also show 1–2-µm-size grains, confirming that grain growth in the N_2 environment is facile in the absence of oxygen and water vapor. When the films are doped with Yb, the grain size decreases significantly ($\sim 100 - 300$ nm) regardless of the annealing environment. This grain growth retardation, even in the N_2-filled GB, suggests that Yb may preferentially segregate to the grain boundaries and slow grain growth just as oxygen does for the undoped films. The grain growth is suppressed even at the lowest Yb-doping levels (2%), and there is little difference in grain sizes even as the Yb concentration increases to 10%.

C. XPS results: Effect of annealing environment on the surface and grain boundaries

XRD, EDS, and SEM show that films with similar compositions, XRD, and microstructure can exhibit significantly different PLQY. This absence of bulk structural and composition differences in films with different PLQYs and changes in PLQY with aging in air implicate surfaces and grain boundaries as having a significant role in determining the PLQY. We thus turn to XPS measurements to provide insight into the effects of the annealing environment on PLQY. Figures 6(a)–6(c) show the XPS Yb 4*d* peak ~184.4 eV for $CsPbCl_3$ films with 5% Yb-doping annealed in three ways (GB, Air, and GB+Air). In the three spectra, we deconvoluted these photoelectrons into three peaks at 187.8, 184.4, and 181.3 eV. The latter is weak, present only in films annealed in air and assigned to Yb° [55,56]. To assign the peaks at 187.8 and 184.4 eV, we turn to the location of Yb 4*d* peaks when Yb is bonded to Cl and O and assume that their location and order of appearance will be similar in $CsPbCl_3$. The Yb 4*d* peaks in $YbCl_3$ and Yb_2O_3 have been reported at 186.6 eV

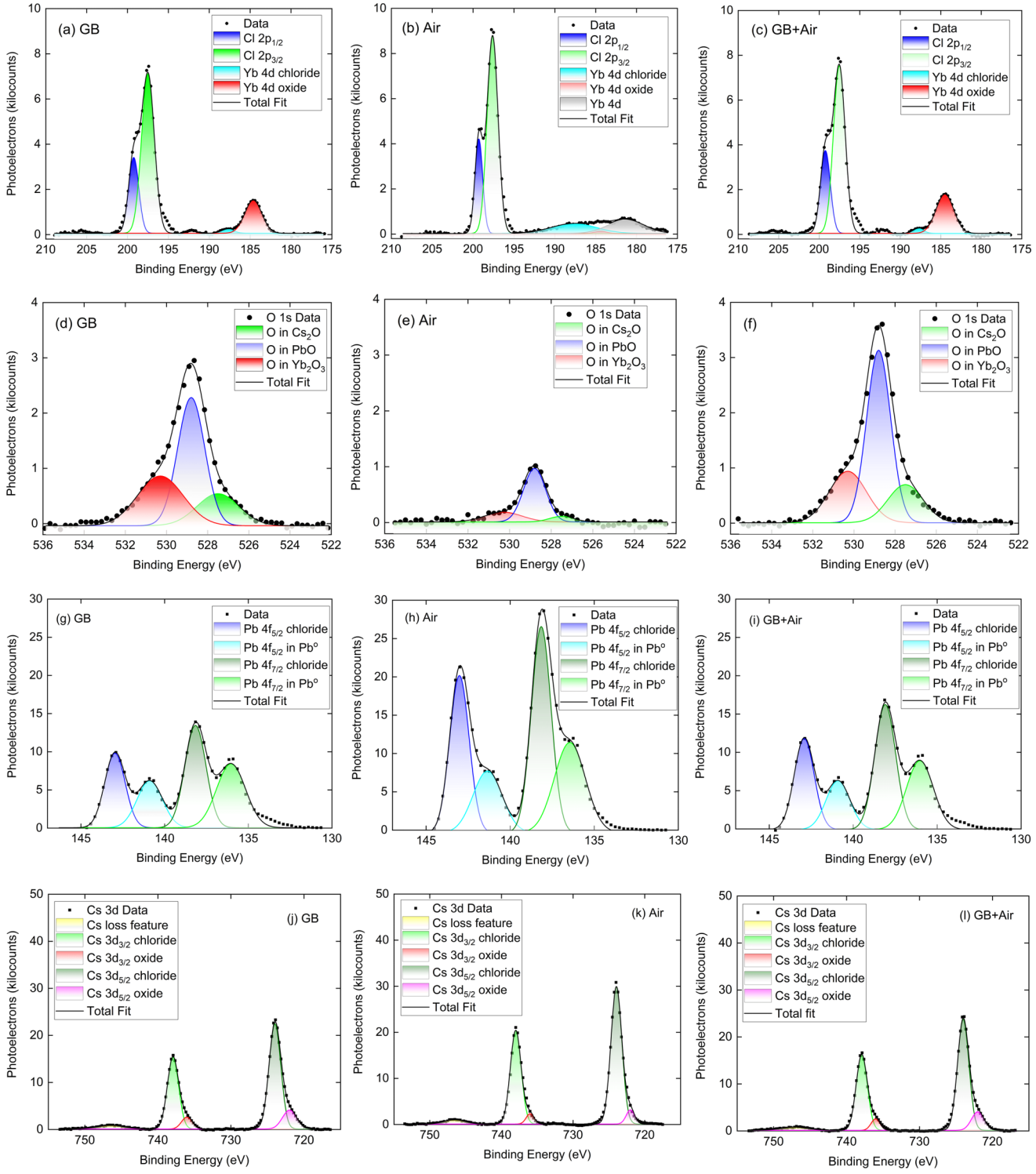

FIG. 6. X-ray photoelectron spectroscopy (XPS) from 5% Yb-doped $CsPbCl_3$ films annealed in three different ways: (1) in a nitrogen-filled glovebox (labeled GB) for 2 h, (2) in the air for 2 h (labeled Air), and (3) in a nitrogen-filled GB for 2 h, followed by further annealing in the air for another 2 h (labeled GB+Air). XPS spectra were taken after sputter cleaning the surface as judged by the disappearance of adventitious carbon. The XPS spectra of as-annealed films before sputter cleaning are in Fig. SI17 in the Supplemental Material [52]. (a)–(c) Cl $2p$ and Yb $4d$ peaks. Cl $2p_{1/2}$ and $2p_{3/2}$ peaks are at 199.3 and 197.6 eV, respectively. Yb $4d$ peaks at 187.8 and 184.4 eV are assigned to Yb bonded to Cl and O, respectively: the Yb $4d$ peak at 181.3 in (b) is assigned to Yb°. (d)–(f) O $1s$ peak. O $1s$ peaks at 530.3, 528.8, and 527.5 eV are assigned to O bonded to Yb, Pb, and Cs, respectively. (g)–(i) Pb $4f$ peaks exhibit spin-orbit splitting (4.87 eV) with each component further split into Pb bonded to Cl (at 138.1 and 143 eV) and Pb° (136.1 and 141 eV). The presence of the Pb° is attributed to its formation by x-ray photolysis during measurement, a well-documented artifact [71]. (j)–(l) Cs $3d$ peaks exhibit spin-orbit splitting (14 eV), with each component further split into Cs bonded to Cl (724 and 738 eV) or bonded to O (722 and 736 eV). The broad weak feature at 747 eV is assigned to plasmon loss.

and between 183.8–185.2 eV, respectively [57–62]. Based on where these peaks are observed in the pure Yb chloride and oxide materials and the expected shifts due to the relative electronegativities of O and Cl, we assign the Yb 4*d* peaks observed at 187.8 and 184.4 eV to Yb bonded to Cl and O, respectively. The 0.8-eV shift from 186.6 eV in $YbCl_3$ to 187.8 eV in $CsPbCl_3$:Yb would be consistent with Yb substituting in the Pb lattice position because Yb is in a more electronegative environment bonded to six Cl atoms than in $YbCl_3$. The Yb oxide 4*d* peak at 184.4 eV is present only when films are annealed in the nitrogen-filled GB or annealed in the GB, followed by in the air (GB+Air). The strengths of these peaks (area under the curve) are similar for films annealed in GB and GB+Air. We detect Yb oxide even in films annealed in an N_2-filled GB with no O_2 or H_2O, indicating that Yb oxidizes when the films are removed from the GB. Surprisingly, however, the Yb 4*d* peak is significantly reduced in films annealed only in the air. A broad and very weak photoelectron signal is attributable to Yb bonded to Cl and Yb$^\circ$ [Fig. 6(b)], but no Yb oxide is detected even after sputtering ∼3 nm off the top of the film. EDS and PL measurements show that Yb is present in all films. We conclude that air-annealing prevents Yb migration to the surface and grain boundaries. Thus, the grain growth during annealing in the air is suppressed by oxidation of the grain boundaries and the surface, not Yb segregation. In contrast, grain growth is suppressed by Yb migrating to the surface and grain boundaries when the film is annealed in an N_2-filled GB.

The XPS from the O 1*s* region corroborates the above conclusion about the suppression of Yb segregation to the surface during air annealing. Before sputtering, XPS data show a strong O 1*s* peak at 531.1 eV from oxygen bound to adventitious carbon and an adventitious C 1*s* peak at 284.4 eV. A second broad peak is at ∼529 eV, which we attribute to metal oxides (e.g., Yb_2O_3, PbO). After sputtering removes the adventitious layer, this second peak is resolved into three others assigned to O bonded to Yb, Pb, and Cs (*vide infra*). XPS data before sputtering are shown in the Supplemental Material [52]. After sputtering, the adventitious carbon peak and O 1*s* peak originating from O bonded to adventitious carbon disappear, revealing three peaks at 527.5, 528.8, and 530.3 eV, assigned to oxygen bound to Cs, Pb, and Yb, based on O 1*s* peaks in Cs_2O [63], PbO [64–66], and Yb_2O_3, respectively [58–62]. Surprisingly, the intensity of the O peak is larger from films annealed in an N_2-filled GB (by a factor of ∼4) than the O peak from films just annealed in air. Again, this indicates that the films are oxidized when removed from the GB. It also indicates that most surface oxygen is bound to Yb_2O_3. When Yb is prevented from segregating to the surface, the amount of O detected on the surface also decreases dramatically. Compare, for example, Figs. 6(b) and 6(e) with Figs. 6(a) and 6(d). When the films are first annealed in the GB, Yb goes to the surfaces and oxidizes upon removing the film to air.

Figures 6(g)–6(i) and 6(j)–6(l) show the Pb 4*f* and Cs 3*d* XPS. We assign the peaks at 138.1 eV [67,68] and 136.1 eV to Pb bonded to Cl and Pb$^\circ$ [69,70]. These are the $4f_{7/2}$ peaks, and a second set spin-orbit split by 4.87 eV is assigned to $4f_{5/2}$. The presence of Pb$^\circ$ is attributed to its formation by x-ray photolysis during measurement, a well-documented artifact [71], and not interpreted further. However, larger Cl-bonded Pb photoelectron intensity in air-annealed films is consistent with low Yb [Fig. 6(b)], low oxygen [Fig. 6(e)], and Pb present in larger concentrations on the surfaces of the air-annealed films. We assign the peaks at 722 and 724 eV to Cs bonded to O and Cl $3d_{5/2}$, respectively. Here, Cs atoms are bonded mostly to Cl and not oxidized significantly. Again, the second set of peaks spin-orbit split by 14 eV is assigned to Cs $3d_{3/2}$ bonded to Cl and O. The XPS data are consistent with the relative thermodynamic stability of the oxides and chlorides of Yb, Pb, and Cs. Of all oxides and chlorides of the elements under consideration, Yb_2O_3 is the most stable ($\Delta G_f^\circ = -1726.8$ kJ/mol), and chlorides of Pb and Cs chlorides are more stable than their oxides. The Gibbs free energies of formation for CsCl, Cs_2O, $PbCl_2$, and PbO are 473.16, −389.6, −399.9, and −219 kJ/mol, respectively. Additional XPS data on Cs, Pb, Yb, O, and C before and after sputtering a thin surface layer to remove adventitious carbon are shown in the Supplemental Material (Figs. SI15–SI17) [52].

D. How do XPS results inform the effect of the annealing environment on PLQY?

Considering the XPS measurements, the PLQY measurements shown in Fig. 3(b) suggest that both Yb migration to the surface and surface oxidation are needed to get the highest PLQY: the highest PLQY is detected in films first annealed in a GB to bring the Yb to the surface and then annealed in the air (i.e., GB+Air) to oxidize the grain boundaries and surfaces to form Yb_2O_3. Some reports on Yb-doped $CsPbCl_3$ hypothesized that NIR emission is enabled by Yb coordinated to the surface of the perovskite nanocrystals, but other work on solution-deposited thin films [13,47,51] and vapor deposition [17,19] has shown evidence that Yb does not need to be on the surface for efficient NIR emission. The absence of the Yb 4*d* peak in the air-annealed films, while there is still NIR emission, provides evidence that the emission in these air-annealed films comes from Yb in the bulk $CsPbCl_3$ and not from the surface. On the other hand, bringing Yb toward the surface is also important. We hypothesize that the extremely high stability of Yb_2O_3 leads to the formation of a surface defect passivating oxide on the $CsPbCl_3$ surfaces and grain boundaries. Thus, processing where Yb is brought to the surface by annealing under N_2 and then oxidizing it in the air provides the best passivation to get maximum NIR PLQY. The PLQY nearly saturates after ∼2% Yb incorporation, suggesting that not all Yb are optically active and that some end up in the oxide on the grain boundaries and surfaces. This is consistent with finding some of the Yb oxidized on the surface. Depending on the annealing environment, Yb diffusing to the surface and oxidizing may leave different amounts of Yb in the grains. Therefore, different amounts of Yb in the grains may cause PLQY differences between GB- and air-annealed films. However, it appears that emission is not limited by Yb availability because PLQY saturates as the nominal amount of Yb increases beyond 2%. Moreover, if the PLQY were limited by the Yb in the grains, we would expect PLQY to be the lowest with the least amount of Yb in the grains, which should correspond to films annealed in the GB, followed by annealing

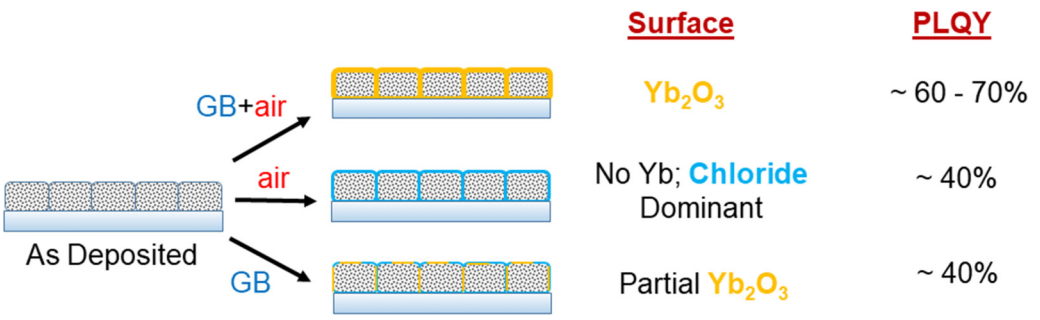

FIG. 7. Illustration of the coverage of Yb-doped $CsPbCl_3$ grain boundaries and surfaces deduced from the x-ray photoelectron spectroscopy (XPS) measurements and summary of the resulting photoluminescence quantum yield (PLQY) values.

in the air. This, however, is not the case. Thus, we attribute the differences in PLQY to differences in surface passivation.

Figure 7 illustrates the grain boundary and surface coverage that emerges from the XPS measurements. When the films are annealed in the air only, Yb is not drawn to the surface, and the surfaces are passivated mostly by Pb and Cs chlorides which are more stable than their oxides. The corresponding PLQY is ∼40% for 2–5% Yb doping. When the films are annealed only in the GB, Yb is brought to the surface and is oxidized when taken out into the air. However, Yb oxidized naturally at room temperature is not as effective as an ytterbium oxide formed upon annealing in air, and the PLQY remains at ∼40%. Only when the Yb on the surface is oxidized by annealing in the air, a robust and passivating layer of Yb_2O_3 formed, and PLQY increases significantly to the 60–70% range. We do not think that Yb in Yb_2O_3 contributes to the NIR emission. Yb_2O_3 has a band gap of 5 eV and does not absorb at the excitation wavelengths (360 nm, 3.4 eV) used in this paper [72]. Thus, the excitons created in $CsPbCl_3$ by absorption must diffuse to the surfaces and then transfer the energy to the Yb in the oxide. Fast nonradiative recombination (<1 ns) in these films makes this an unlikely mechanism. Perhaps the strongest reason to discount this possibility is the efficient PLQY from air-annealed films that do not show a significant amount of Yb_2O_3 on their surfaces.

IV. SUMMARY AND CONCLUSIONS

We used PVD to deposit Yb-doped $CsPbCl_3$ thin films with nominal Yb doping up to 10%. These films have an absorption onset at ∼2.95 eV and show weak excitonic band-edge emission at 425 nm. The films also show strong NIR PL centered at 985 nm originating from the Yb $^2F_{5/2} \rightarrow {}^2F_{7/2}$ transition. The highest PLQY of the NIR peak was 69.7% from the films with 2.5% Yb that were annealed in an N_2-filled GB for 2 h and then annealed in the air for 2 h, both at 350 °C. Here, Yb incorporation and annealing environment do not significantly affect the XRD patterns of $CsPbCl_3$ films, but Yb incorporation does suppress grain growth. Similarly, annealing in the air and oxidation of the grain boundaries suppresses grain growth, leading to grains of a few hundred nanometers. PLQY is sensitive to the state of the surfaces, which in turn is sensitive to the annealing environment. XPS measurements revealed that annealing in N_2 brings Yb to the surface of the films, which then oxidizes when the films are annealed in the air to form a robust ytterbium oxide that passivates surface defects. This results in the highest NIR PLQY values (60–70%). In contrast, annealing in the air suppresses Yb migration to the surface. The chloride-passivated surface results in lower NIR PLQY values (∼40%). Figure 7 summarizes the principal finding of this paper.

Finally, the PLQY of vapor-deposited Yb-doped $CsPbCl_3$ thin films is lower than the PLQY of nanocrystals. Two possible reasons are that either thin films have more defects that act as nonradiative recombination centers than nanocrystals or exciton confinement improves PL. These reasons are consistent with higher visible PL from undoped $CsPbCl_3$ nanocrystals than from undoped $CsPbCl_3$ thin films. For example, $CsPbCl_3$ nanocrystals have shown visible PLQY as high as 60% with PL lifetimes >10 ns, while the $CsPbCl_3$ thin films have PLQY <1% and PL lifetimes <1 ns [73].

ACKNOWLEDGMENTS

The X-ray microdiffractometer with GADDS was acquired through the support of the National Science Foundation under Award No. CRIF/CHE-0840277 and the NSF MRSEC Program under Award No. DMR-0820341. In addition, the authors acknowledge the use of shared facilities provided through the Materials Research Science and Engineering Center (MRSEC) and MRI programs of the National Science Foundation under Awards No. DMR-1420073 and No. DMR-0923251. We gratefully acknowledge support for instrument use and scientific and technical assistance from the Surface Science Core Facilities at Advanced Science Research Center of CUNY. Work by H.K. was partially supported by the Schlumberger Foundation Faculty for the Future Program. E.S.A. gratefully acknowledges support from the Alstadt Lord Mark Chair.

[1] L. Protesescu, S. Yakunin, M. I. Bodnarchuk, F. Krieg, R. Caputo, C. H. Hendon, R. X. Yang, A. Walsh, and M. V. Kovalenko, Nano Lett. **15**, 3692 (2015).

[2] N. Li, Z. Zhu, J. Li, A. K. -Y. Jen, and L. Wang, Adv. Energy Mater. **8**, 1800525 (2018).
[3] J. de Roo, M. Ibáñez, P. Geiregat, G. Nedelcu, W. Walravens, J. Maes, J. C. Martins, I. van Driessche, M. V. Kovalenko, and Z. Hens, ACS Nano **10**, 2071 (2016).
[4] X. Qiu, B. Cao, S. Yuan, X. Chen, Z. Qiu, Y. Jiang, Q. Ye, H. Wang, H. Zeng, J. Liu *et al.*, Sol. Energ. Mater. Solar C. **159**, 227 (2017).
[5] J. Maes, L. Balcaen, E. Drijvers, Q. Zhao, J. de Roo, A. Vantomme, F. Vanhaecke, P. Geiregat, and Z. Hens, J. Phys. Chem. Lett. **9**, 3093 (2018).
[6] N. Pandey, A. Kumar, and S. Chakrabarti, RSC Adv. **9**, 29556 (2019).
[7] G. H. Ahmed, J. K. El-Demellawi, J. Yin, J. Pan, D. B. Velusamy, M. N. Hedhili, E. Alarousu, O. M. Bakr, H. N. Alshareef, and O. F. Mohammed, ACS Energy Lett. **3**, 2301 (2018).
[8] C. M. Sutter-Fella, Y. Li, M. Amani, J. W. Ager, F. M. Toma, E. Yablonovitch, I. D. Sharp, and A. Javey, Nano Lett. **16**, 800 (2016).
[9] Y. Kim, E. Yassitepe, O. Voznyy, R. Comin, G. Walters, X. Gong, P. Kanjanaboos, A. F. Nogueira, and E. H. Sargent, ACS Appl. Mater. Interfaces **7**, 25007 (2015).
[10] S. L. Abiodun, P. J. Pellechia, and A. B. Greytak, J. Phys. Chem. C **125**, 3463 (2021).
[11] S. E. Creutz, R. Fainblat, Y. Kim, M. C. de Siena, and D. R. Gamelin, J. Am. Chem. Soc. **139**, 11814 (2017).
[12] T. J. Milstein, D. M. Kroupa, and D. R. Gamelin, Nano Lett. **18**, 3792 (2018).
[13] D. M. Kroupa, J. Y. Roh, T. J. Milstein, S. E. Creutz, and D. R. Gamelin, ACS Energy Lett. **3**, 2390 (2018).
[14] T. J. Milstein, K. T. Kluherz, D. M. Kroupa, C. S. Erickson, J. J. de Yoreo, and D. R. Gamelin, Nano Lett. **19**, 1931 (2019).
[15] T. A. Cohen, T. J. Milstein, D. M. Kroupa, J. D. MacKenzie, C. K. Luscombe, and D. R. Gamelin, J. Mater. Chem. A **7**, 9279 (2019).
[16] C. S. Erickson, M. J. Crane, T. J. Milstein, and D. R. Gamelin, J. Phys. Chem. C **123**, 12474 (2019).
[17] M. J. Crane, D. M. Kroupa, J. Y. Roh, R. T. Anderson, M. D. Smith, and D. R. Gamelin, ACS Appl. Energy Mater. **2**, 4560 (2019).
[18] M. J. Crane, D. M. Kroupa, and D. R. Gamelin, Energy Environ. Sci. **12**, 2486 (2019).
[19] D. M. Kroupa, M. J. Crane, and D. R. Gamelin, Single-source flash sublimation of metal-halide semiconductors, in Physical Chemistry of Semiconductor Materials and Interfaces XVIII (2019).
[20] D. M. Kroupa, M. J. Crane, J. S. Silvia, and D. R. Gamelin, Ray-tracing analysis of module-level power generation from quantum-cutting ytterbium-doped metal-halide perovskites, in 2020 47th IEEE Photovoltaic Specialists Conference (PVSC) (2020).
[21] J. Y. D. Roh, M. D. Smith, M. J. Crane, D. Biner, T. J. Milstein, K. W. Krämer, and D. R. Gamelin, Phys. Rev. Mater. **4**, 105405 (2020).
[22] D. E. Sommer, D. R. Gamelin, and S. T. Dunham, Phys. Rev. Mater. **6**, 025404 (2022).
[23] M. N. Tran, I. J. Cleveland, G. A. Pustorino, and E. S. Aydil, J. Mater. Chem. A. **9**, 13026 (2021).
[24] K. T. Kluherz, S. T. Mergelsberg, D. E. Sommer, J. Y. D. Roh, S. A. Saslow, D. Biner, K. W. Krämer, S. T. Dunham, J. J. de Yoreo, and D. R. Gamelin, Phys. Rev. Mater. **6**, 074601 (2022).
[25] M. N. Tran, I. J. Cleveland, J. R. Geniesse, and E. S. Aydil, Mater. Horiz. **9**, 2191 (2022).
[26] M. N. Tran, I. J. Cleveland, and E. S. Aydil, ACS Appl. Electron. Mater. **4**, 4588 (2022).
[27] G. Pan, X. Bai, D. Yang, X. Chen, P. Jing, S. Qu, L. Zhang, D. Zhou, J. Zhu, W. Xu *et al.*, Nano Lett. **17**, 8005 (2017).
[28] T. Cai, J. Wang, W. Li, K. Hills-Kimball, H. Yang, Y. Nagaoka, Y. Yuan, R. Zia, and O. Chen, Adv. Sci. **7**, 2001317 (2020).
[29] N. Chen, T. Cai, W. Li, K. Hills-Kimball, H. Yang, M. Que, Y. Nagaoka, Z. Liu, D. Yang, A. Dong *et al.*, ACS Appl. Mater. Interfaces **11**, 16855 (2019).
[30] N. Ding, W. Xu, D. Zhou, Y. Ji, Y. Wang, R. Sun, X. Bai, J. Zhou, and H. Song, Nano Energy **78**, 105278 (2020).
[31] D. L. Dexter, J. Chem. Phys. **21**, 836 (1953).
[32] P. Vergeer, T. J. H. Vlugt, M. H. F. Kox, M. I. den Hertog, J. P. J. M. van der Eerden, and A. Meijerink, Phys. Rev. B **71**, 014119 (2005).
[33] D. L. Dexter, Phys. Rev. **108**, 630 (1957).
[34] Y. Zhydachevskyy, I. I. Syvorotka, V. Tsiumra, M. Baran, L. Lipińska, A. Wierzbicka, and A. Suchocki, Sol. Energ. Mater. Sol. C. **185**, 240 (2018).
[35] Y. Tai, X. Li, X. Du, B. Pan, and G. Yuan, RSC Adv. **8**, 23268 (2018).
[36] J. Ueda and S. Tanabe, J. Appl. Phys. **106**, 043101 (2009).
[37] B. M. van der Ende, L. Aarts, and A. Meijerink, Adv. Mater. **21**, 3073 (2009).
[38] B. M. van der Ende, L. Aarts, and A. Meijerink, Phys. Chem. Chem. Phys. **11**, 11081 (2009).
[39] R. Martín-Rodríguez, R. Geitenbeek, and A. Meijerink, J. Am. Chem. Soc. **135**, 13668 (2013).
[40] D. Zhou, D. Liu, G. Pan, X. Chen, D. Li, W. Xu, X. Bai, and H. Song, Adv. Mater. **29**, 1704149 (2017).
[41] X. Zhang, Y. Zhang, X. Zhang, W. Yin, Y. Wang, H. Wang, M. Lu, Z. Li, Z. Gu, and W. W. Yu, J. Mater. Chem. C **6**, 10101 (2018).
[42] X. Luo, T. Ding, X. Liu, Y. Liu, and K. Wu, Nano Lett. **19**, 338 (2019).
[43] D. Zhou, R. Sun, W. Xu, N. Ding, D. Li, X. Chen, G. Pan, X. Bai, and H. Song, Nano Lett. **19**, 6904 (2019).
[44] S. Zhao, Y. Zhang, and Z. Zang, Chem. Commun. **56**, 5811 (2020).
[45] Y. Zhu, G. Pan, L. Shao, G. Yang, X. Xu, J. Zhao, and Y. Mao, J. Alloys Compd. **835**, 155390 (2020).
[46] R. Sun, D. Zhou, P. Lu, X. Jing, X. Zhuang, S. Liu, Y. Wang, X. Bai, W. Xu, and H. Song, Nano Energy **93**, 106815 (2022).
[47] A. Ishii and T. Miyasaka, Adv. Sci. **7**, 1903142 (2020).
[48] J.-P. Ma, Y.-M. Chen, L.-M. Zhang, S.-Q. Guo, J.-D. Liu, H. Li, B.-J. Ye, Z.-Y. Li, Y. Zhou, B.-B. Zhang *et al.*, J. Mater. Chem. C **7**, 3037 (2019).
[49] K. Momma and F. Izumi, J. Appl. Crystallogr. **44**, 1272 (2011).
[50] M. R. Linaburg, E. T. McClure, J. D. Majher, and P. M. Woodward, Chem. Mater. **29**, 3507 (2017).
[51] A. Ishii and T. Miyasaka, J. Chem. Phys. **153**, 194704 (2020).
[52] See Supplemental Material at https://link.aps.org/supplemental/10.1103/PhysRevMaterials.7.065404 for details on film thickness calculations; PL and UV-vis absorption data, PLQY data,

XRD patterns, and SEM micrographs not shown in the main text; and XPS spectra of the films prior to sputtering.

[53] S. W. Eaton, M. Lai, N. A. Gibson, A. B. Wong, L. Dou, J. Ma, L.-W. Wang, S. R. Leone, and P. Yang, Proc. Natl. Acad. Sci. **113**, 1993 (2016).

[54] P. Patnaik, *Handbook of Inorganic Chemicals*, 1st ed. (McGraw-Hill, New York, 2002).

[55] S. B. M. Hagström, P. O. Hedén, and H. Löfgren, Solid State Commun. **8**, 1245 (1970).

[56] S. P. Kowalczyk, N. Edelstein, F. R. McFeely, L. Ley, and D. A. Shirley, Chem. Phys. Lett. **29**, 491 (1974).

[57] Y. Uwamino, A. Tsuge, T. Ishizuka, and H. Yamatera, Bull. Chem. Soc. Jpn. **59**, 2263 (1986).

[58] Y. Uwamino, T. Ishizuka, and H. Yamatera, J. Electron. Spectros. Relat. Phenom. **34**, 67 (1984).

[59] B. D. Padalia, W. C. Lang, P. R. Norris, L. M. Watson, and D. J. Fabian, Proc. R. Soc. Lond. A **354**, 269 (1977).

[60] D. D. Sarma and C. N. R. Rao, J. Electron. Spectros. Relat. Phenom. **20**, 25 (1980).

[61] A. F. Orchard and G. Thornton, J. Electron. Spectros. Relat. Phenom. **13**, 27 (1978).

[62] A. Kahraman, H. Karacali, and E. Yilmaz, J. Alloys. Compd. **825**, 154171 (2020).

[63] S. Yang and C. W. Bates, Appl. Phys. Lett. **36**, 675 (1980).

[64] J. A. Taylor and D. L. Perry, J. Vac. Sci. Technol. A **2**, 771 (1984).

[65] D. S. Zingg and D. M. Hercules, J. Phys. Chem. **82**, 1992 (1978).

[66] K. S. Kim, T. J. O'Leary, and N. Winograd, Anal. Chem. **45**, 2214 (1973).

[67] Y.-W. Peng, C.-P. Wang, G. Kumar, P.-L. Hsieh, C.-M. Hsieh, and M. H. Huang, ACS Sustain. Chem. Eng. **10**, 1578 (2022).

[68] L. R. Pederson, J. Electron. Spectros. Relat. Phenom. **28**, 203 (1982).

[69] J. F. McGilp, P. Weightman, and E. J. McGuire, J. Phys. C: Solid State **10**, 3445 (1977).

[70] A. B. Mandale and S. Badrinarayanan, J. Electron. Spectros. Relat. Phenom. **53**, 87 (1990).

[71] J. D. McGettrick, K. Hooper, A. Pockett, J. Baker, J. Troughton, M. Carnie, and T. Watson, Mater. Lett. **251**, 98 (2019).

[72] C. Zhang, X. Wang, L. Liang, H. Yuan, J. Qi, Z. Liao, and T. Lu, J. Alloys Compd. **907**, 164454 (2022).

[73] Y. Zhang, X. Cheng, D. Tu, Z. Gong, R. Li, Y. Yang, W. Zheng, J. Xu, S. Deng, and X. Chen, Angew. Chem. Int. Ed. **60**, 9693 (2021).